Elliptic-type soliton combs in optical ring microresonators

Rodrigues D. Dikandé Bitha[*] and Alain M. Dikandé[†]

Laboratory of Research on Advanced Materials and Nonlinear Science (LaRAMaNS), Department of Physics,
Faculty of Science, University of Buea, P.O. Box 63 Buea, Cameroon

Soliton crystals are periodic patterns of multispot optical fields formed from either time or space entanglements of equally separated identical high-intensity pulses. These specific nonlinear optical structures have gained interest in recent years with the advent and progress in nonlinear optical fibers and fiber lasers, photonic crystals, wave-guided wave systems, and most recently optical ring microresonator devices. In this work an extensive analysis of characteristic features of soliton crystals is carried out, with an emphasis on their one-to-one correspondence with elliptic solitons. With this purpose in mind, we examine their formation, their stability, and their dynamics in ring-shaped nonlinear optical media within the framework of the Lugiato-Lefever equation. The stability analysis deals with internal modes of the system via a 2×2-matrix Lamé-type eigenvalue problem, the spectrum of which is shown to possess a rich set of bound states consisting of stable zero-frequency modes and unstable decaying as well as growing modes. Turning towards the dynamics of elliptic solitons in ring-shaped fiber resonators with Kerr nonlinearity, we first propose a collective-coordinate approach, based on a Lagrangian formalism suitable for elliptic-soliton solutions to the nonlinear Schrödinger equation with an arbitrary perturbation. Next we derive time evolutions of elliptic-soliton parameters in the specific context of ring-shaped optical fiber resonators, where the optical field evolution is thought to be governed by the Lugiato-Lefever equation. By solving numerically the collective-coordinate equations an analysis of the amplitude, the position, the phase of internal oscillations, the phase velocity, the energy, and phase portraits of the amplitude is carried out and reveals a complex dynamics of the elliptic soliton in ring-shaped optical microresonators. Direct numerical simulations of the Lugiato-Lefever equation are also carried out seeking for stationary-wave solutions, and the numerical results are in very good agreement with the collective-coordinate approach.

I. INTRODUCTION

Since the observation of solitons in optical fibers and fiber lasers [1], the optical communication technology has experienced tremendous progress along with a wealth of modern techniques for information processings and data manipulations. This progress led, among others, to current techniques of optimized data compression out of which the techniques of time, wavelength, polarization, and phase multiplexings [2]. In fiber communication technology, however, the spatial dimension has been a relatively less relevant issue until the revolution triggered by the advent of photonic crystals [1,3], and the recent appearance of optical frequency combs (OFCs) in fiber lasers [4,5]. On this last point, photonic crystals can support hundreds of spatial modes, a feature which could be exploited for the propagation of OFCs in form of space-division multiplexed (SDM) signals. Indeed the development of systems using space-division multiplexing in photonic crystals, offers a promising technological tool for increasing the capacity of optical networks, namely by increasing the volume of information per fiber. Note that fibers supporting several spatial modes provide the most effective means to increase the fiber-based information capacity, given that the capacity increases with the number of modes in the absence of mode-dependent losses.

OFCs [4,5] are the most recent revolution in the fiber laser technology, these are discrete high-intensity optical spectra of equidistant phase-locked lines extending over a broad spectral range [4]. Since their discovery, they have been reported in various nonlinear optical media such as semiconductor microresonators [6] and fiber-laser cavities. They offer wide-range applications in telecommunication for the generation of high-repetition rate picosecond pulses, namely for ultra-high capacity transmission systems based on optical division multiplexing [7–9]. OFCs today are widely used in spectroscopy [4], astronomy, metrology, frequency synthesis, optical clocking [10,11], and so on.

The mechanism by which optical soliton frequency combs are generated, as well as their stability, have been some of most active aspects in recent theoretical and experimental researches in nonlinear optics [12–14]. Mode-locking has emerged as the likely mechanism. It consists of the generation of a uniform train of optical solitons formed from a four-wave mixing process, associated with the nonlinear interaction between light and the bulk material of a whispering gallery mode microresonator. Depending on the frequency and power of the pump laser, mode-locking can lead to the excitation of equally spaced optical soliton lines thus forming what is usually termed "soliton Kerr combs" [15–18].

In view of the periodic structure of optical soliton Kerr combs generated by space-division multiplexing in the

---

[*]rodrigue.donald@ubuea.cm
[†]dikande.alain@ubuea.cm

microresonator cavity, one might be tempted to think of its possible connection with the so-called soliton crystals [19–22], which also has been of considerable interest in the recent past in harmonic-mode-locked fiber lasers. The idea has indeed been recently introduced in a recent experimental study by Cole *et al.* [23], who reported the observation of spontaneously and collectively ordered ensembles of copropagating solitons, whose spatial discretizations allow their temporal separations within monolithic Kerr microresonator cavities. Relevant to stress, concerning a discrete ordering of some collection of several solitons to form a soliton-crystal structure, it has been established [24] that soliton crystals can result from a spatial or temporal entanglement of equidistant pulses. Quite remarkably, the resulting crystal-like ordered soliton field obeys the cubic nonlinear Schrödinger equation (NLSE), i.e., the same equation governing the spatiotemporal evolution of its elementary (i.e., pulse) constituents. On the other hand, the dynamics of soliton combs in Kerr microresonators are thought to be governed by the Lugiato-Lefever equation (LLE) [25], which is actually a perturbed NLSE. Therefore whether soliton-crystal structures and soliton Kerr combs are connected, and if so in which way they could be connected, is a relevant issue for a better understanding of the process underlying the soliton frequency comb generation and its robustness *vis à vis* external factors such as cavity losses, external detunings and so on.

In this work we propose an extensive analysis of the above issue by addressing three key aspects, namely the build-up (i.e., formation) mechanism and characteristic features of the soliton-crystal structure, its stability *vis à vis* scattering with continuous-wave radiations, and finally the effects of cavity loss and a detuning pump on the soliton-crystal profile, within the framework of the LLE.

In Sec. II, we present the perturbed NLSE specifically named LLE and discuss its soliton solutions in the absence of perturbations. Thus we first consider the artifical pulse-lattice pattern proposed by Herr *et al.* [26], represented as a discrete series of fundamental sech-shaped pulses in the angular-coordinates representation. We show that this artificial structure is equivalent to a space-division multiplexing of identical pulses [24,27–29], and obeys the same NLSE governing the dynamics of its single-pulse constituents. As a sequel of the established one-to-one correspondance between the soliton-crystal structure of Ref. [26] and the elliptic-soliton solution to the NLSE, we derive characteristic parameters of the soliton crystals namely its period, amplitude, and pulse separation, as a function of fundamental parameters of the individual pulse constituents. In Sec. III we introduce an approach to the linear stability analysis for elliptic solitons. The approach rests on a mapping of the soliton crystal-small amplitude waves scattering problem onto a 2×2 matrix eigenvalue problem involving two coupled Lamé equations [30]. The matrix eigenvalue problem yields a rich and varied discrete spectrum comprising internal modes, growing modes, and decaying modes. Spectral parameters of these modes, i.e., their eigenvalues and eigenfunctions, are determined analytically. In Sec. IV we discuss the dynamics of soliton frequency combs within the framework of the collective-coordinate approach for elliptic-soliton solution to the LLE. We first construct a general collective-coordinate theory using a Lagrangian formalism for

elliptic-soliton solutions of the cubic NLSE with an arbitrary perturbation, and then derive the collective-coordinate equations for elliptic-soliton parameters in the specific context of the LLE. In Sec. V these collective-coordinate equations are solved numerically with the help of a sixth-order Runge-Kutta algorithm [31,32], combined with a 3/8 Simpson rule for finite integrals, which also enables us to explore some relevant characteristic features of the system dynamics, namely the phase portraits and the energy of elliptic solitons. Section VI is devoted to concluding remarks.

II. MODEL, SOLITON CRYSTALS, AND ELLIPTIC SOLITONS

The dynamics of soliton Kerr combs in ring-shaped optical microresonators is usually described by the LLE, which is a perturbed NLSE given by [25]

$$i\frac{\partial \psi}{\partial \tau} - \frac{\beta_2}{2}\frac{\partial^2 \psi}{\partial \theta^2} + \gamma|\psi|^2\psi = -i(\alpha_1 + i\alpha_2)\psi + iF, \quad (1)$$

where $\psi = \psi(\tau,\theta)$ is the slow-varying envelope of the field, θ is the angular coordinate in the ring microresonator, and τ is time. β_2 is the group-velocity dispersion (GVD) of the microresonator, γ is the nonlinear (i.e., Kerr) coefficient, α_1 is the linear loss (damping term), α_2 is the pump detuning frequency, and F is the pump field intensty. In all the following we focus on the anomalous dispersion regime, i.e., $\beta_2 < 0$.

In this section we are interested in the solution to the LLE for $\alpha_1 = \alpha_2 = F = 0$. In this case Eq. (1) reduces to the cubic NLSE

$$i\frac{\partial \psi}{\partial \tau} - \frac{\beta_2}{2}\frac{\partial^2 \psi}{\partial \theta^2} + \gamma|\psi|^2\psi = 0. \quad (2)$$

Seeking for stationary solutions to the above equation, we assume an optical field $\psi(\tau,\theta)$ of the following form [24]:

$$\psi(\tau,\theta) = a(\theta)e^{i\beta\tau}, \quad (3)$$

where β is the envelope modulation frequency and $a(\theta)$ is the amplitude of the field envelope assumed real. Substituting Eq. (3) in Eq. (2) yields

$$-\beta a - \frac{\beta_2}{2}\frac{\partial^2 a}{\partial \theta^2} + \gamma a^3 = 0, \quad (4)$$

which can be transformed into the energy-integral equation

$$\left(\frac{da}{d\theta}\right)^2 = -\frac{2\beta}{\beta_2}a^2 + \frac{\gamma}{\beta_2}a^4 + C. \quad (5)$$

The integration constant C determines profiles of the amplitude $a(\theta)$. The first physical context of interest is that of a localized profile, where the field envelope $a(\theta)$ has a vanishing shape as $\theta \to \pm\infty$ such that $C = 0$. This leads to the pulse soliton solution

$$a(\theta) = \sqrt{\frac{2\beta}{\gamma}}\text{sech}\left[\sqrt{\frac{-2\beta}{\beta_2}}\theta\right]. \quad (6)$$

Physically the solution (6) describes a high-intensity single-pulse signal of amplitude $a_0 = \sqrt{\frac{2\beta}{\gamma}}$ and width $\ell_0 = \sqrt{\frac{\beta_2}{-2\beta}}$.

When $C \neq 0$, localized structures become unstable and no pulse can form. Nevertheless the NLSE still admits
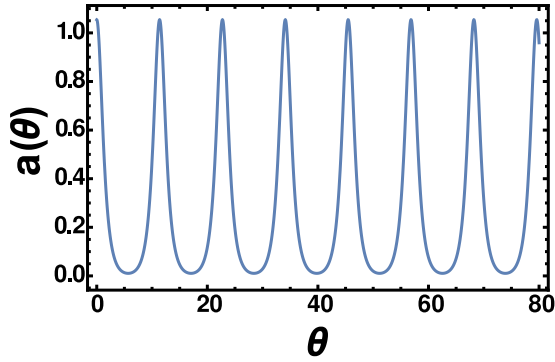
FIG. 1. Elliptic-soliton solution to the NLSE: $\beta_2 = -0.5$, $\beta = 0.5$ and $\gamma = 0.9$, $\kappa = 0.97$.

nonlinear-wave solutions. Indeed, for finite nonzero values of C, Eq. (5) is an elliptic first-order differential equation admitting a solution [24,33–36]

$$a(\theta) = \frac{a_0}{\sqrt{2 - k^2}} dn\left[\frac{\theta}{\sqrt{2 - k^2}\ell_0}, \kappa\right], \qquad (7)$$

where dn is a Jacobi elliptic function of modulus κ ($0 \leqslant \kappa \leqslant 1$). The spatial profile of the envelope solution Eq. (7) is plotted in Fig. 1 for $\beta_2 = -0.5$, $\beta = 0.5$, $\gamma = 0.9$, and $\kappa = 0.97$ (values chosen for illustration).

The figure suggests a comb structure consisting of a periodic network of pulse-shaped signals, where the periodic nature of the pulse comb is actually characteristic of the Jacobi elliptic function dn which is periodic in its argument with a period

$$\theta_p = 2K\sqrt{2 - \kappa^2}\ell_0, \qquad (8)$$

with $K = K(\kappa)$ the elliptic integral of first kind. This period, which we assimilate to the pulse spatial repetition rate in the soliton-comb pattern, appears to be proportional to the width of individual pulses. It is also worth remarking that according to formula (7), the pulse amplitude in the pulse comb is smaller. In the limit $\kappa \to 1$ the spatial repetition rate θ_p becomes infinite and the elliptic-soliton solution (7) decays into the single-pulse solution (6).

To probe the inner structure of the artificial soliton-crystal pattern proposed in Ref. [26], in the light of the two distinct exact soliton solutions to the NLSE obtained above, we remark that the authors suggested that the soliton crystal formed by SDM of pulses in microresonators could readily be represented as [26]

$$a(\theta) = \sum_J C_j \text{sech}\left(\sqrt{\frac{2(\omega_0 - \omega_p)}{D_2}}(\theta - \theta_j)\right), \qquad (9)$$

$$D_2 = -\frac{c}{n_0} D_1^2 \beta_2, \qquad (10)$$

where θ_j is the angular position of the jth pulse, while ω_0 and ω_p are, respectively, the resonance frequency of the resonator and the pump Laser frequency. n_0 is the refractive index, D_1 is the free spectral range, and D_2 is the resonator anomalous dispersion. In Eq. (9) each pulse soliton is regarded as an eigenfunction with a normalized amplitude C_j representing an existing mode within the soliton comb. In the specific case

when pulses are identical such that $C_j = C_0$, and moreover are equally spaced such that $\theta_j = j\theta_0$, the SDM soliton crystal Eq. (9) reduces to

$$a(\theta) = C_0 \sum_J \text{sech}\left(\sqrt{\frac{2(\omega_0 - \omega_p)}{D_2}}(\theta - j\theta_0)\right), \qquad (11)$$

where θ_0 is the pulse repetition rate. If the series (11) corresponds to a comb of sech-type pulses in which constituents are solutions to the NLSE, then in terms of the single-pulse solution (6) we can set

$$\beta = \frac{n_0}{cD_1^2}(\omega_0 - \omega_p), \quad C_0 = \sqrt{\frac{2\beta}{\gamma}}. \qquad (12)$$

In this case the sum in Eq. (11) becomes exact if we assume an infinitely large ensemble of pulses giving [24]

$$a(\theta) = \theta_H C_0 dn\left[\frac{\theta}{\ell_H}, \kappa\right], \qquad (13)$$

$$\theta_H = \frac{2K'}{\pi} C_0, \quad \ell_H = \frac{\pi}{2K'}\sqrt{\frac{D_2}{2(\omega_0 - \omega_p)}}, \qquad (14)$$

where $K' = K(1 - \kappa^2)$. It turns out that the spatial multiplex of sech pulses (11) is nothing else but an elliptic soliton, and as such it is a soliton crystal equivalent to the elliptic-soliton solution (7) of the NLSE with a spatial repetition rate θ_0 given by

$$\theta_0 = 2K\ell_H, \qquad (15)$$

where ℓ_H, the pulse width in the comb structure, has been defined in formula (14).

The elliptic solitons (7) or (13) form a multisoliton complex that decay into a harmonic wavepacket when $\kappa \to 0$. When $\kappa \to 1$, both reduce to a single-pulse field. In the context of laser applications they exhibit interesting features among which the dependence of their amplitude on both the coupled resonance width and the pulse repetition rate. As it is apparent from formula (15), the pulse repetition rate is relevant in the sense that it determines the existence and stability of the soliton crystal in the ring resonator device: the smaller the pulse repetition rate the larger the pulse amplitude. Also, according to the above relations, the elliptic soliton amplitude is inversely proportional to the cavity resonance width β as defined in Eq. (12). Consequently, the elliptic soliton envelope should be widened as the amplitude grows, thereby reducing collisions between pulses in th soliton-comb structure.

III. SOLITON CRYSTAL STABILITY

The stability of nonlinear signals in optical media is a key requirement for their processing, storage or transmission. While the issue has been investigated at length for single-pulse solutions (see, e.g., Ref. [37]), recent interest in multiplexed solitons has shifted attention to the stability of these particular structures from both experimental [26] and theoretical standpoints within the framework of the linear stability analysis [29].

In this section we wish to investigate the stability of soliton crystals, represented by elliptic solitons as established

in the previous section. In this purpose we consider small-amplitude noises in the ring microresonator propagating together with the elliptic-soliton signal. For the sake of formal mathematical analysis, we shall deal with the elliptic soliton (7) obtained as exact solution to the NLSE (2). In the presence of small-amplitude noises this solution now becomes

$$\psi(\tau,\theta) = \{a(\theta) + [u(\theta) - v(\theta)]e^{i\omega\tau}$$
$$+ [u^*(\theta) + v^*(\theta)]e^{-i\omega\tau}\}e^{i\beta\tau}, \quad (16)$$

where $a(\theta)$ is the elliptic-soliton envelope given by Eq. (7), while $u(\theta)$ and $v(\theta)$ are the spatial amplitudes of two complex noise fields having a common frequency ω [37]. Substituting Eq. (16) in the NLSE (2), and keeping only linear terms in $u(\theta)$ and $v(\theta)$, we find the following set of coupled Lamé [30] equations:

$$\left[\frac{\partial^2}{\partial\varphi^2} + 2dn^2(\varphi) + \varepsilon\right]v + \nu u = 0, \quad (17)$$

$$\left[\frac{\partial^2}{\partial\varphi^2} + 6dn^2(\varphi) + \varepsilon'\right]u + \nu v = 0, \quad (18)$$

with $\varphi = \sqrt{-\frac{2\beta}{\beta_2(2-\kappa^2)}}\theta$, $\varepsilon=\varepsilon'=(2 - \kappa^2)\beta$, and $\nu=(2 - \kappa^2)\omega$. The set Eqs. (17) and (18) can be mapped onto a 2×2-matrix linear eigenvalue problem with eigenfunctions forming a family of two-component complex vectors (u, v), whose eigenvalues are the couples of scalars $(\varepsilon, \varepsilon')$. In matrix form the eigenvalue problem reads

$$\mathbf{H}\mathbf{U} = \varepsilon(\kappa)\mathbf{U}, \quad (19)$$

where

$$\mathbf{H} = \begin{bmatrix} \frac{\partial^2}{\partial\varphi^2} + 2dn^2(\varphi) & \nu \\ \nu & \frac{\partial^2}{\partial\varphi^2} + 6dn^2(\varphi) \end{bmatrix}, \quad \mathbf{U} = \begin{bmatrix} v \\ u \end{bmatrix}.$$

We look for solutions to the above matrix eigenvalue problem, which are linear combinations of the exact eigenfunctions of Eqs. (17) and (18) in the absence of coupling. To find these exact eigenfunctions we remark that for $\omega = 0$, i.e., when the noise fields are in steady state, the set Eqs. (17) and (18) bursts into two independent Lamé equations: the first becomes a Lamé equation of first order and the second to a Lamé equation of second order. Instructively, an nth-order Lamé eigenvalue problem has the general form [24,38,39]

$$-\left[\frac{\partial^2}{\partial z^2} + n(n+1)\kappa^2 sn^2(z)\right]\psi(z) = \lambda(\kappa)\psi(z), \quad (20)$$

where sn is a Jacobi elliptic function and n a positive integer. Considering the discrete spectrum of this eigenvalue equation, it is known that for a given value of n the Lamé equation possesses exactly $2n + 1$ bound-state solutions. For Eqs. (17) and (18) this leads to the eigenfunctions listed in Tables I and II, together with their corresponding eigenvalues.

When $\omega \neq 0$, solutions to the coupled eigenvalue Eqs. (17) and (18) are vectors $[u(\varphi), v(\varphi)]$ whose components are orthogonal linear combinations of the two-component basis vector $u_0(\varphi)$, $v_0(\varphi)$, which are exact eigenmodes given in Tables I and II. Two new basis vectors ensuing from the

TABLE I. Eigenvalues $\varepsilon(\kappa)$ and eigenfunctions $v(\varphi)$ of the first-order Lamé equation (17), when $\omega = 0$. $v_0^{(i)}$ are normalization constants.

Eigenvalues	Eigenfunctions
$\varepsilon(\kappa) = (1 + \kappa^2)$	$v^{(1)}(\kappa) = v_0^{(1)} sn(\varphi)$
$\varepsilon(\kappa) = 1$	$v^{(2)}(\kappa) = v_0^{(2)} cn(\varphi)$
$\varepsilon(\kappa) = \kappa^2$	$v^{(3)}(\kappa) = v_0^{(3)} dn(\varphi)$

requirement of an orthonormalized basis for the two coupled Lamé equations (17) and (18) are

$$\begin{bmatrix} a_1 \\ 1 \end{bmatrix} cn(\varphi)e^{i\eta} + \begin{bmatrix} 0 \\ b_1 \end{bmatrix} sn(\varphi)dn(\varphi)e^{i\eta},$$

$$\begin{bmatrix} a_2 \\ 1 \end{bmatrix} sn(\varphi)e^{i\eta} + \begin{bmatrix} 0 \\ b_2 \end{bmatrix} cn(\varphi)dn(\varphi)e^{i\eta},$$

where the functions $f(x,\kappa) = \{cn(x),sn(x)\}$ and $g_i(x,\kappa) = \{sn(x)dn(x),cn(x)dn(x)\}$ should be mutually orthogonal, i.e.,

$$\int_{-K}^{K} f_i(x,\kappa)g_i(x,\kappa)dx = 0. \quad (21)$$

In this new two-component basis we obtain the following solutions.

(1) On the basis $[cn(x),sn(x)dn(x)]$:

$$v(\varphi) = \mp\frac{i\kappa}{\sqrt{1-\kappa^2}}cn(\varphi,\kappa)e^{2i\sqrt{1-\kappa^2}\varphi}, \quad (22)$$

$$u(\varphi) = \left[cn(\varphi,\kappa) + \frac{i}{\sqrt{1-\kappa^2}}sn(\varphi,\kappa)dn(\varphi,\kappa)\right]e^{2i\sqrt{1-\kappa^2}\varphi}, \quad (23)$$

with spectral parameters

$$\nu(\kappa) = \mp 2i\kappa\sqrt{1-\kappa^2}, \quad \varepsilon(\kappa) = 1 - 2\kappa^2. \quad (24)$$

(2) On the basis $[sn(x),cn(x)dn(x)]$:

$$v(\varphi) = \pm sn(\varphi,\kappa)e^{2i\varphi}, \quad (25)$$

$$u(\varphi) = [sn(\varphi,\kappa) \mp i cn(\varphi,\kappa)dn(\varphi,\kappa)]e^{2i\varphi}, \quad (26)$$

TABLE II. Eigenvalues $\varepsilon'(\kappa)$ and eigenfunctions $u(\varphi)$ of the second-order Lamé equation (18), when $\omega = 0$. $\kappa_1^2 = 1 - \kappa^2$, $u_0^{(i)}$ are normalization constants.

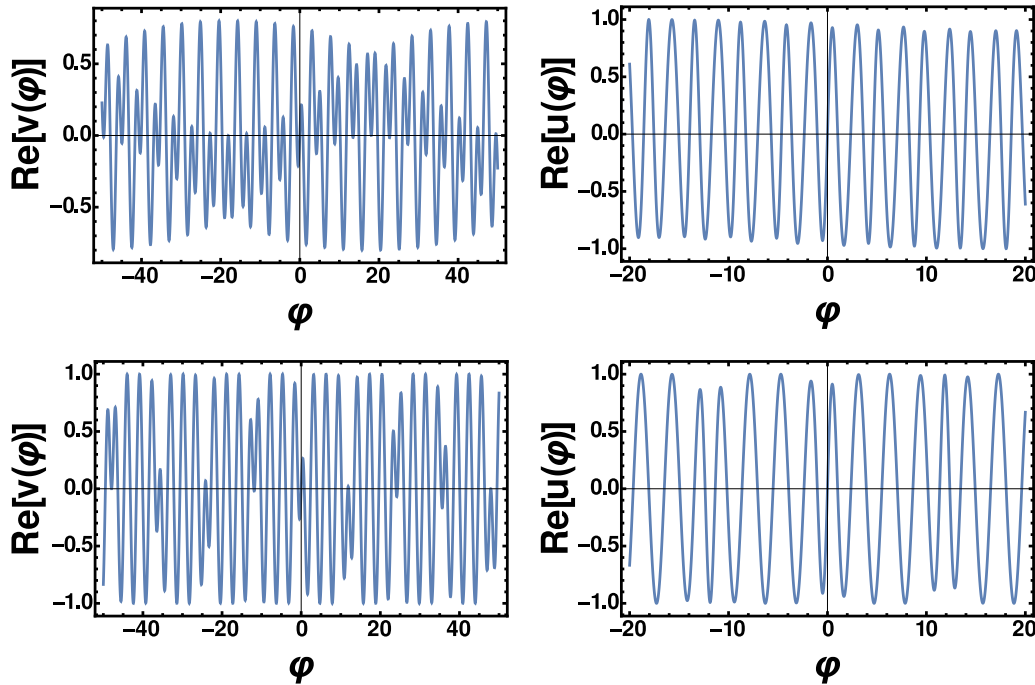| Eigenvalues	Eigenfunctions
$\varepsilon'(\kappa) = (4 + \kappa^2)$	$u^{(1)}(\kappa) = u_0^{(1)} sn(\varphi)cn(\varphi)$
$\varepsilon'(\kappa) = (1 + 4\kappa^2)$	$u^{(2)}(\kappa) = u_0^{(2)} sn(\varphi)dn(\varphi)$
$\varepsilon'(\kappa) = (1 + \kappa^2)$	$u^{(3)}(\kappa) = u_0^{(3)} cn(\varphi)dn(\varphi)$
$\varepsilon'(\kappa) = 2[(1 + \kappa^2) \mp \sqrt{1 - \kappa^2\kappa_1^2}]$	$u^{(4,5)}(\kappa) = u_0^{(4,5)} sn^2(\varphi) - u_0^{4,5}$
	$\times \frac{(1+\kappa^2)\pm\sqrt{1-\kappa^2\kappa_1^2}}{3k^2}$

FIG. 2. Real parts of the internal modes $v(\varphi)$ (left) and $u(\varphi)$ (right) given in (25) and (26). Top: $\kappa = 0.8$, bottom: $\kappa = 97$.

for which the spectral parameters are

$$\nu(\kappa) = \pm 2\kappa, \quad \varepsilon(\kappa) = 1 + \kappa^2. \tag{27}$$

According to Eq. (24) eigenvalues of the internal modes (22) to (23) are purely imaginary, therefore these modes will either decay or grow and hence are unstable. We refer to the internal mode with a growing amplitude as "growing modes," whereas the internal mode with decreasing amplitude is referred to as "decaying modes." In fact their instability affects the elliptic-soliton stability, indeed the ansatz formula (16) clearly shows that the exponential growth or decay of internal modes are the result of a combination with the exponential modulation of the Elliptic soliton envelope $a(\varphi)$. On the contrary eigenvalues of the pair of internal modes (25) to (26) are real, as evidenced by formula (27). Hence they are stable bound states, coexisting with the elliptic soliton, but distinct from the elliptic soliton by their amplitudes and frequencies. They can be regarded as long-term (i.e., nonlinear) periodic oscillations in the elliptic-

soliton background. Their amplitudes are represented in Fig. 2, while their eigenvalues are sketched in Fig. 3.

IV. DYNAMICS OF ELLIPTIC SOLITONS IN RING MICRORESONATORS: COLLECTIVE COORDINATE APPROACH

A. Collective-coordinate equations for the general perturbed NLSE

Unlike the NLSE for which the elliptic-soliton solution has been obtained in Sec. II and shown to be equivalent to a pulse-shaped soliton comb, the LLE Eq. (1) is a member of a wide family of inhomogeneous NLSEs which are usually not exactly integrable [40,41]. Nevertheless, an approximate solution for this last equation can be obtained by means of a perturbation theory, such as the collective-coordinate method which is more explicitly an adiabatic perturbation theory. While this method has been widely utilized for perturbed NLSEs in the context of single-pulse soliton [41], the possible existence of multipulse
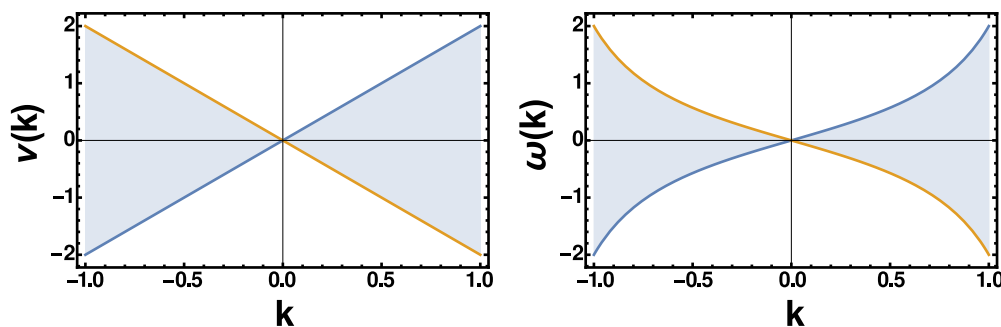

FIG. 3. Plots of the internal-mode eigenvalues ν (right) and ω (left) given by (27), as a function of the Jacobi elliptic modulus κ. In the two plots the shaded region (blue region in color) denotes the stability domain.

solutions and particularly soliton-crystal solutions to the same equations recently motivated its extension [27] to these particular physical contexts. To start we shall construct the collective-coordinate theory for the Elliptic-soliton solution to the NLSE with an arbitrary perturbation, and next apply the theory to the LLE.

Consider the perturbed cubic NLSE

$$i\frac{\partial \psi}{\partial t} + \frac{1}{2}\frac{\partial^2 \psi}{\partial \vartheta^2} + \gamma |\psi|^2 \psi(t,\vartheta) = i\epsilon Q[\psi, \psi^{(n,m)}], \quad (28)$$

where $\epsilon Q(\psi, \psi^{(n,m)})$ represents the perturbation and $\psi^{(n,m)}$ refer to the nth and mth derivatives of $\psi(t,\vartheta)$ with respect to t and ϑ, respectively. Let the elliptic-soliton solution to Eq. (28) be of a general form

$$\psi(t,\vartheta) = \eta(t)dn\{\eta(t)[\vartheta - q(t)]\}\exp[i\phi(t) - \delta(t)\vartheta], \quad (29)$$

where $\eta(t)$ is the amplitude, $q(t)$ is the position, $\phi(t)$ is the phase of internal oscillations, and $\delta(t)$ is the phase velocity of the elliptic soliton. Our aim is to determine the set of differential equations governing time evolutions of these four collective-coordinate variables. Within the framework of the Lagrangian formalism [27], we define the Lagrangian density associated to the perturbed Eq. (28) as:

$$l_d = \frac{i}{2}(\psi \psi_t^* - \psi_t \psi^*) - \frac{1}{2}(|\psi|^4 - |\psi_t|^2) + xi(\epsilon Q \psi^* - \epsilon Q^* \psi), \quad (30)$$

where the subscripts refer to derivatives with respect to the variable. The Lagrangian L can be computed via the formula

$$L = \int_{-K}^{K} l_d \, d\vartheta, \quad (31)$$

which after the substitution of Eq. (29) and integration yields

$$L = (\phi_t - \delta_t q)\eta E - \frac{4}{3}(2 - \kappa^2)\eta^3 E + \eta[(2 - \kappa^2)\eta^2 + \delta^2]E + i\int_{-K}^{K}(\epsilon Q \psi^* - \epsilon Q^* \psi)d\vartheta, \quad (32)$$

where E is the elliptic integral of second kind. Applying the Lagrangian formalism with respect to the four collective-coordinate variables on L [27], we obtain the following set of coupled first-order time ordinary differential equations

$$\eta_t = \frac{1}{E}\text{Re}\int_{-K}^{K}\epsilon Q(\psi)\psi \, d\vartheta, \quad (33)$$

$$\delta_t = -\frac{\kappa^2}{E}\text{Im}\int_{-K}^{K}sn[\eta(\vartheta - q)]\epsilon Q(\psi)\psi \, d\vartheta, \quad (34)$$

$$q_t = -\delta + \frac{1}{\eta^2 E}\text{Re}\int_{-K}^{K}(\vartheta - q)\epsilon Q(\psi)\psi \, d\vartheta, \quad (35)$$

$$\phi_t = \frac{1}{E}\text{Im}\int_{-K}^{K}\epsilon Q(\psi)\left\{\frac{1}{\eta}\psi^* - \kappa^2(\vartheta - q)sn[\eta(\vartheta - q)]\right. \\ \left. \times \psi_{cn}^*\right\}d\vartheta + \frac{1}{2}[(2 - \kappa^2)\eta^2 - \delta^2] + q\delta_t. \quad (36)$$

In the last set we defined

$$\psi_{cn}(t,\vartheta) = \eta(t)cn\{\eta(t)[\theta - q(t)]\}\exp[i\phi(t) - \delta(t)\vartheta], \quad (37)$$

while "Re" and "Im" stand for the real and imaginary parts, respectively.

B. Collective-coordinate equations for the LLE

By setting $t = \frac{\gamma}{2}\tau$ and $\vartheta = \sqrt{\frac{\gamma}{2|\beta_2|}}\theta$, the LLE Eq. (1) can be expressed as the perturbed NLSE Eq. (28) with

$$\epsilon Q(\psi) = f - \frac{2}{\gamma}(\alpha_1 + i\alpha_2)\psi(t,\vartheta), \quad (38)$$

where $f = \frac{2}{\gamma}F$. Replacing Eq. (38) in the set Eqs. (33) to (36) we obtain

$$\eta_t = -2\alpha_r \eta + \frac{2f}{E}\cos(\delta q - \phi)\int_0^K dn(\vartheta)\cos\left(\frac{\delta}{\eta}\vartheta\right)d\vartheta, \quad (39)$$

$$\delta_t = -\frac{2\kappa^2}{E}f\cos(\delta q - \phi)\int_0^K dn(\vartheta)sn(\vartheta)\sin\left(\frac{\delta}{\eta}\vartheta'\right)d\vartheta, \quad (40)$$

$$q_t = -\delta - \frac{2f}{\eta^3 E}\sin(\delta q - \phi)\int_0^K \vartheta dn(\vartheta)\sin\left(\frac{\delta}{\eta}\vartheta\right)d\vartheta, \quad (41)$$

$$\phi_t = -2\alpha_i - \frac{\alpha_i}{E}[E - (1 - \kappa^2)K] + \frac{2f}{\eta E}\sin(\delta q - \phi) \\ \times \int_0^K dn(\vartheta)\cos\left(\frac{\delta}{\eta}\vartheta'\right)d\vartheta - \frac{2\kappa^2}{\eta E}f\cos(\delta q - \phi) \\ \times \int_0^K cn(\vartheta)sn(\vartheta)\sin\left(\frac{\delta}{\eta}\vartheta\right)d\vartheta \\ + \frac{1}{2}[(2 - \kappa^2)\eta^2 - \delta^2] + q\delta_t, \quad (42)$$

where we define $\alpha_r = \frac{2\alpha_1}{\gamma}$, $\alpha_i = \frac{2\alpha_2}{\gamma}$. In the next section we present numerical simulations of the collective-coordinate equations (39) to (42), and explore some important aspects of the system dynamics including the phase portraits and the energy of the elliptic soliton for some values of the perturbation parameters.

V. NUMERICAL RESULTS

The collective-coordinate equations (39) to (42) were solved numerically using a sixth-order Runge-Kutta scheme [31,32], in conjunction with a 3/8 Simpson rule for the integrals. The Jacobi elliptic functions dn, sn, and cn were generated numerically by employing an algorithm proposed in Ref. [42]. In all our simulations we considered $\kappa = 0.97$, $\gamma = 1$, and $F = 0.01$.

Figure 4 shows time series of the amplitude $\eta(t)$, the position $q(t)$, the phase of internal oscillations $\phi(t)$. and the phase velocity $\delta(t)$ of the elliptic soliton, obtained numerically for $\alpha_1 = 0.001$ and $\alpha_2 = 0.5$. A main dominant behavior of characteristic parameters of the elliptic soliton emerging from the figures is a damped oscillation, except the position which is only very slightly oscillating and suggests more a linear acceleration. The time series of the amplitude seems more appealing and informative about the elliptic soliton stability,
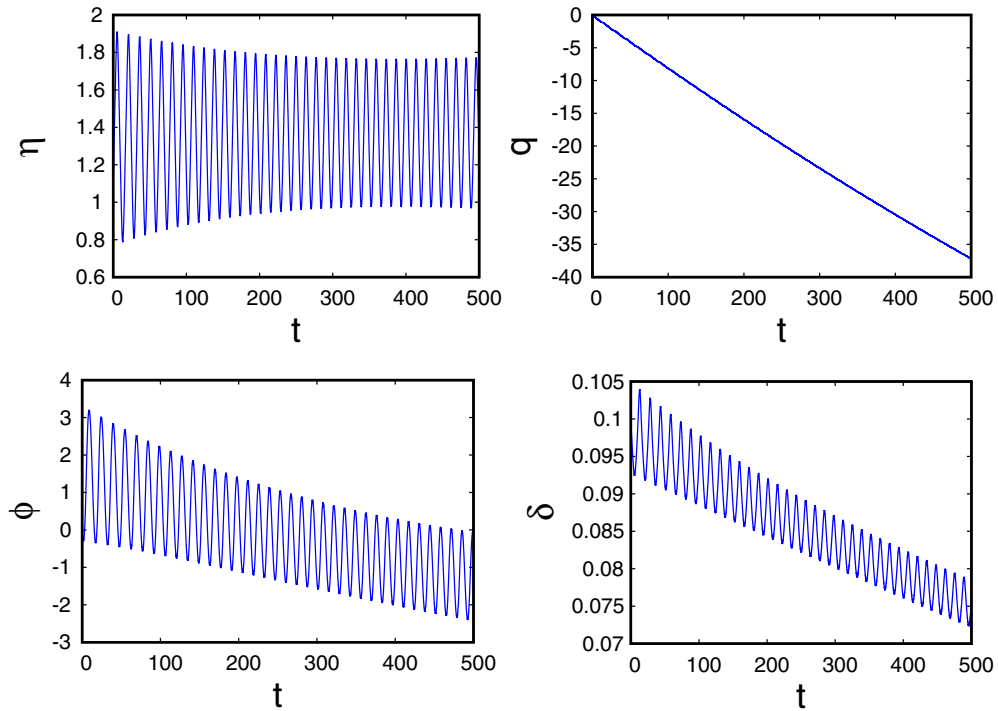
FIG. 4. Time evolutions of the elliptic-soliton parameters $\eta(t)$, $q(t)$, $\phi(t)$, and $\delta(t)$ for $\alpha_1 = 0.001$ and $\alpha_2 = 0.5$.

so we followed the evolution of this specific parameter for different combinations of the two perturbation coefficients α_1 and α_2. In particular Fig. 5 represents the time evolution of $\eta(t)$ for a fixed value of α_2 but varying α_1, whereas in Fig. 6 α_1 is

kept fix but α_2 is varied. If the exponentially damped oscillating behavior remains most dominant, the two figures clearly suggest that the linear loss coefficient α_1 effectively controls the elliptic soliton stability while an increase in α_2 enhances
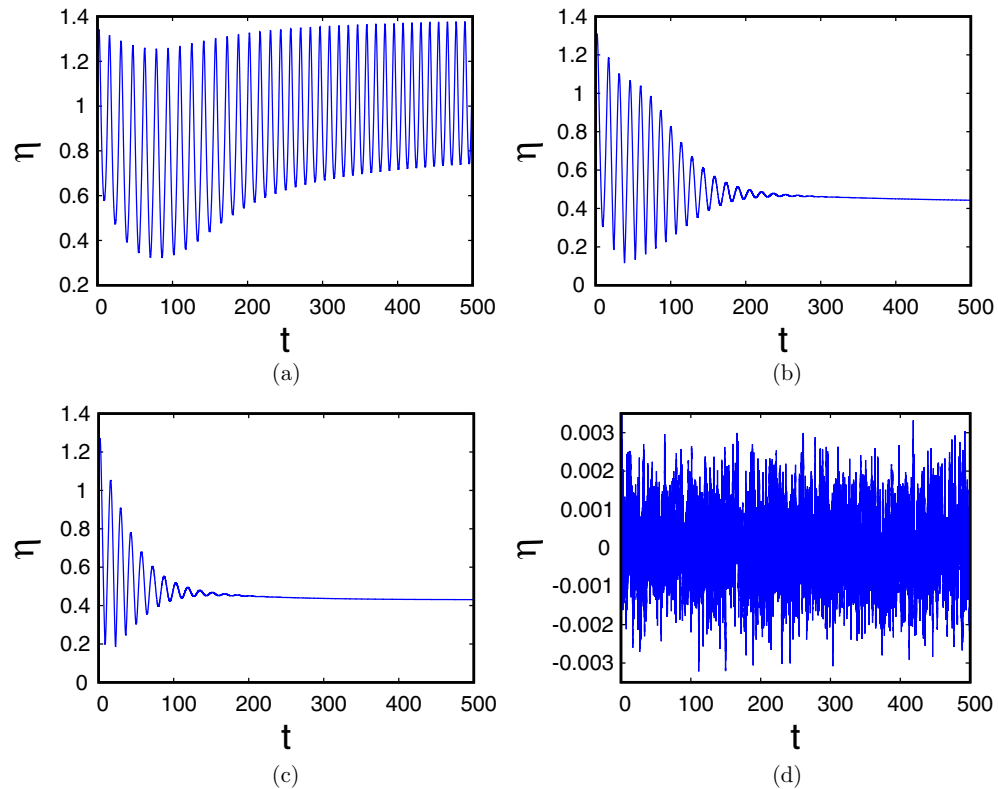

FIG. 5. Time evolutions of the elliptic-soliton amplitude $\eta(t)$ for $\alpha_2 = 0.01$. From (a) to (d): $\alpha_1 = 0.001$, $\alpha_1 = 0.005$ $\alpha_1 = 0.01$, $\alpha_1 = 1$.
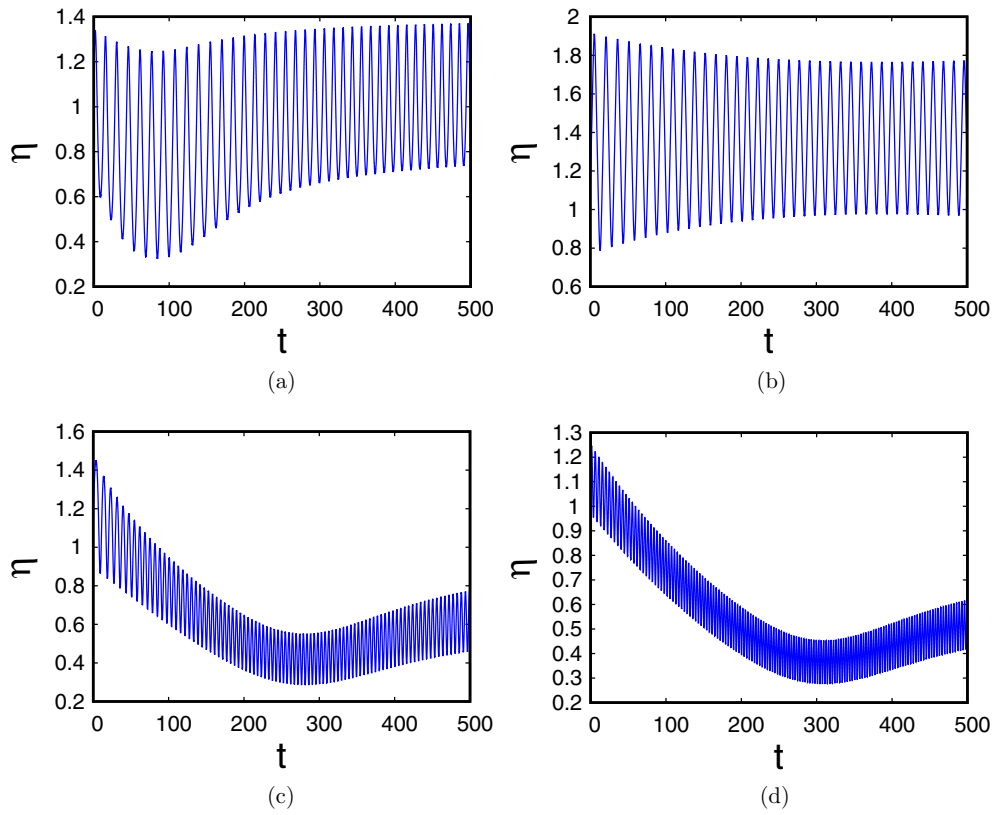
FIG. 6. Time evolutions of the elliptic-soliton amplitude $\eta(t)$, for $\alpha_1 = 0.001$. From (a) to (d): $\alpha_2 = 0.005$, $\alpha_2 = 0.5$, $\alpha_2 = 1$, $\alpha_2 = 1$.

the oscillatory feature of its amplitude. The apparent control of the elliptic-soliton stability by the linear loss coefficient α_1 has an important implication as concerns the dynamics of optical

soliton frequency combs. Indeed, besides characterizing noise in the phase spectrum of the soliton and thus affecting its repetition frequency, the quality factor Q (a dimensionless
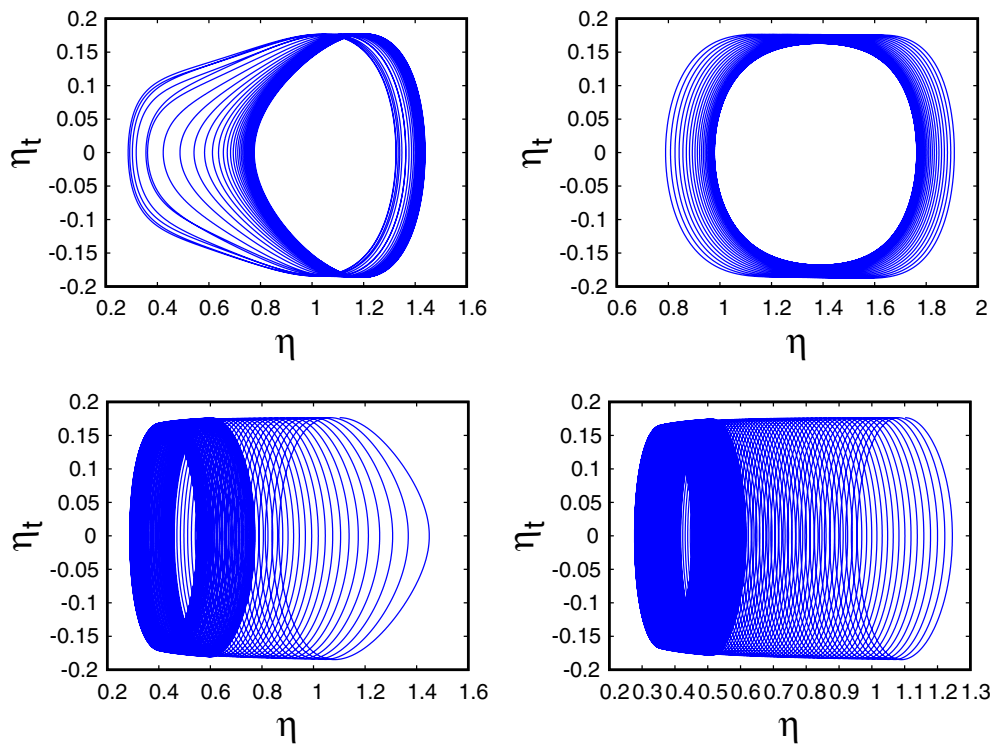

FIG. 7. Phase portraits of the amplitude for $\alpha_1 = 0.001$. From top to bottom and from left to right: $\alpha_2 = 0.05$, $\alpha_2 = 0.5$, $\alpha_2 = 0.7$, $\alpha_2 = 1$.
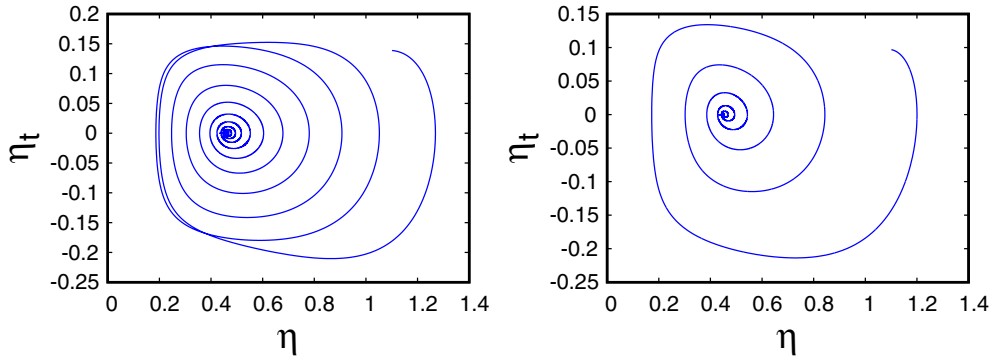
FIG. 8. Phase portraits of the amplitude for $\alpha_2 = 0.01$ and $\alpha_1 = 0.005$ (left), $\alpha_1 = 0.01$ (right).

parameter describing how underdamped a resonator is) of the microresonator is inversely proportional to the microresonator loss coefficient. This means that the average lifetime of a comb structure in the soliton state will depend on the linear loss: when the linear loss of the cavity is increased, the soliton comb should fade away more or less shortly after its emission. On the contrary, a decrease in the linear loss will enhance the signal intensity in the cavity. The later phenomenon is quite common in laser processings and is known as Q switching. Note that at very high values of the linear loss α_1, compared to the pump detuning frequency α_2, the evolution of the soliton comb becomes chaotic as seen in Fig. 5(d).

The changes observed in Fig. 6 on the time-series evolution of the elliptic soliton amplitude due to a variation of the pump detuning frequency α_2, suggest a very rich dynamics of the

system related to this parameter. To this last point, Fig. 6 shows that as we increase α_2 we move from regularly oscillating elliptic-soliton structures to "rolling" patterns [Figs. 6(c) and 6(d)]. This behavior is more apparent by looking at the phase portrait of the amplitude, which we represented in Fig. 7 for a fixed value of α_1. For values of α_2 around 1 and above, the three-dimensional representation of the elliptic-soliton amplitude exhibits a spin-like behavior. Note that these patterns are in agreement with experiments [14,18,43], where it is observed that roll patterns are formed when the resonator is pumped above a certain threshold.

To provide a more global picture of the temporal evolution of the elliptic-soliton amplitude in the LLE, we also plotted the phase portrait for varying loss coefficient α_1 and fixed pump detuning frequency α_2. Figure 8 are plots of these phase
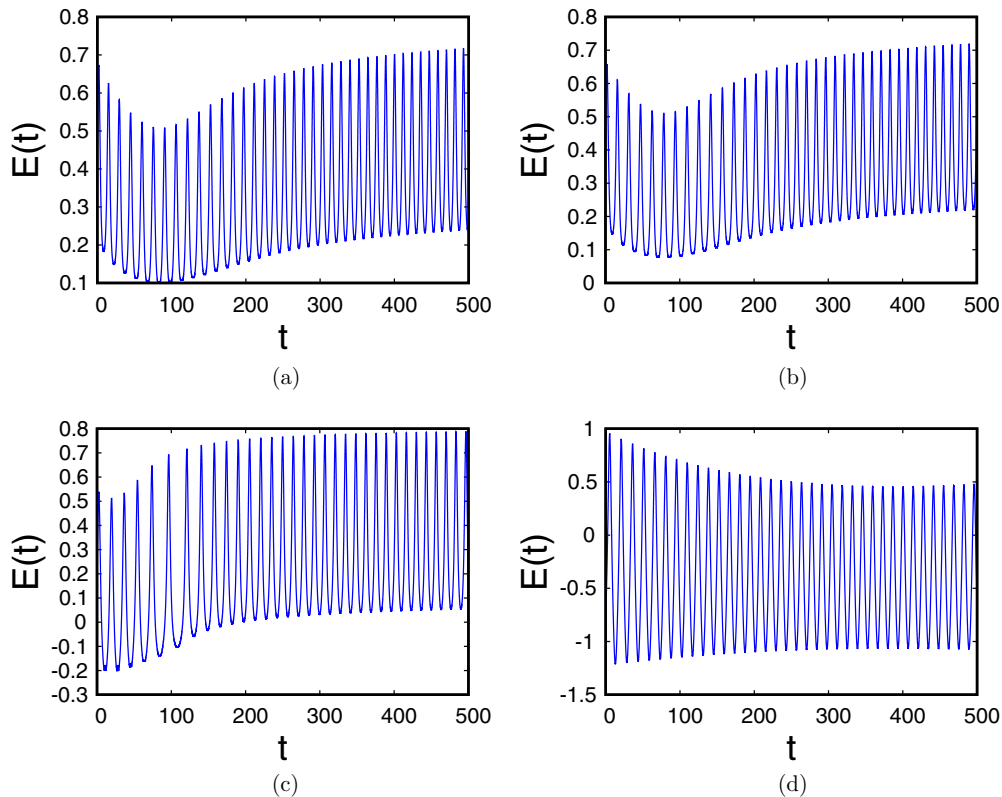

FIG. 9. Time variation of the elliptic-soliton energy. From graphs (a) to (f) the linear loss parameter is constant (i.e., $\alpha_1 = 0.001$), while the pump detuning frequency is varied as: (a) $\alpha_2 = 0.001$, (b) $\alpha_2 = 0.01$, (c) $\alpha_2 = 0.1$, (d) $\alpha_2 = 0.5$.
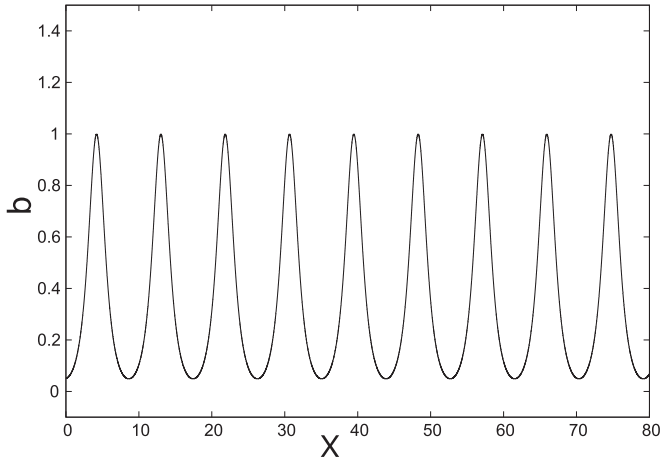
FIG. 10. Soliton-crystal profiles from numerical simulations for $F_0 = \alpha_1 = \alpha_2 = 0$.

portraits. Essentially Fig. 8 suggests that when the coefficient of linear loss α_1 is increased, the oscillatory feature of the eliptic-soliton amplitude in the resonator cavity tends to die down, thus confirming the stabilizing role played by this parameter in the elliptic-soliton dynamics.

In the final analysis we examine the time variation of the "topological" energy of the elliptic soliton, considered as another relevant indicator of the soliton-comb stability as it propagates in the ring microresonator. In our analysis we consider numerical results only for variations of the pump detuning frequency, avoiding chaotic evolutions by fixing the linear loss coefficient in the regime of regular motion.

We derive the energy from the Lagrangian using the general relation

$$E = \left(\sum_i \dot{q}_i \frac{\partial}{\partial \dot{q}_i} - 1 \right) L, \tag{43}$$

where q_i is one of the collective-coordinate variables η, q, ϕ, δ. With the help of Eq. (32), we find the energy

$$E = \frac{4}{3}(2 - \kappa^2)\eta^3 E(\kappa) - \eta[(2 - \kappa^2)\eta^2 + \delta^2]E(\kappa)$$
$$+ 2Im \int_{-K}^{K} \varepsilon \psi^* d\vartheta. \tag{44}$$

The time variation of the elliptic-soliton energy is depicted in Fig. 9, for some values of linear loss and the pump detuning frequency. The figures show that as one increases the pump detuning frequency, a second oscillatory curve shows up which overtakes gradually the elliptic-soliton energy. This second energy may be attributed to the emergence of roll patterns in the system. When $\alpha_2 > 0.6$, the roll patterns completely wipe out solitonic structures in the system.

Before closing this section, we find it worth checking the consistency of our assumption in the choice of Eq. (29) as an appropriate variational solution to the LLE. Indeed, we assume that profile of the soliton-crystal structure (7) was preserved within the framework of the LLE, except its characteristic parameters that were expected to change in time due to the perturbations. To this end we will solve the LLE numerically, putting particular emphasis on its stationary-wave solutions.

As already stressed above, the LLE is a perturbed NLSE and in this respect can be simulated, from a general standpoint, using the split-step Fourier transform scheme [44]. This algorithm combines a standard numerical scheme for ordinary differential equations in one of the two coordinates, and a numerical spectral transform in the other coordinate of the equation. More explicitly, for Eq. (1) the split-step scheme will combine a spatial integration using any classic algorithm for ordinary-differential equation as, for instance, the Runge-Kutta scheme, whereas the time derivative is treated by means of Fourier transform. Most generally the split-step Fourier transform will give rise to a traveling-wave solution, which is expected to reproduce more or less accurately the exact analytical pulse solution.

In our specific context, however, we are concerned with stationary waves, which we believe provide a better representation of the soliton-crystal structure observed experimentally [23,26]. To check that Eq. (29) is an appropriate choice for variational soliton-crystal-type solution for the LLE, we simulated Eq. (1) seeking for stationary-wave solutions. To this end, it is useful to remark that such solutions should be in the following general form:

$$\psi(\tau, \theta) = a_0 \, b[X(\theta)]e^{i\beta\tau},$$
$$X(\theta) = \sqrt{-\frac{2\beta}{\beta_2}}\theta, \quad a_0 = \sqrt{\frac{2\beta}{\gamma}}. \tag{45}$$
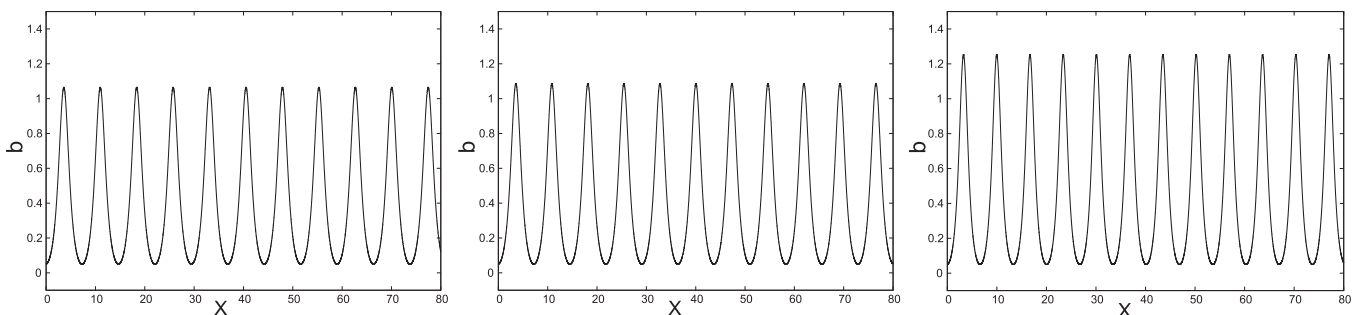

FIG. 11. Soliton-crystal profiles from numerical simulations for $F_0 = 0.1$, $\beta\tau = 0.5$, and $\alpha_1 = 0.1$. α_2 is varied as 0.05 (left graph), 0.1 (middle graph), and 0.5 (right graph).
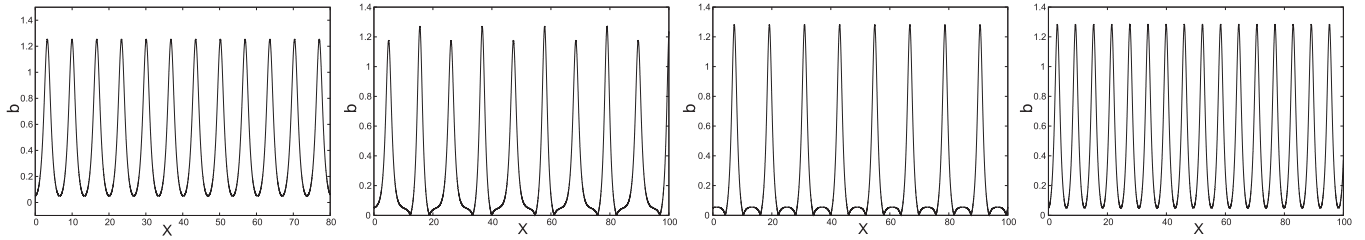
FIG. 12. Oscillating amplitude, width, and repetition rate of pulses in the soliton-crystal structure, as suggested by direct numerical simulations of Eq. (46) at different times τ. $F_0 = 0.1$, $\alpha_1 = 0.1$, $\alpha_2 = 0.5$ and from left to right: $\beta\tau = 0.5, 10, 15,$ and 20.

Substituting Eq. (45) in Eq. (1), and imposing that $b[X(\theta)]$ should be a real function, we obtain

$$-b + b_{XX} + 2b^3 = (-i\alpha_1 - \alpha_2)b + i\frac{F}{\beta}\sqrt{\frac{\gamma}{2\beta}}\, e^{-i\beta\tau}, \quad (46)$$

where

$$F_0 = \frac{F}{\beta}\sqrt{\frac{\gamma}{2\beta}}, \;\; \alpha_0 = \sqrt{\alpha_1^2 + \alpha_2^2}, \;\; \xi = \arctan(\alpha_1/\alpha_2). \quad (47)$$

Equation (46) provides the accurate representation of the stationary profile of nonlinear solutions to Eq. (1). We simulated Eq. (46) for some couples of values of (α_1, α_2), at selected (i.e., fixed) times τ. First we consider the soliton-crystal profile suggested by numerical simulations in the absence of perturbations (i.e., $\alpha_1 = 0$, $\alpha_2 = 0$, $F = 0$), which we represented in Fig. 10. Next we consider numerical solutions in the presence of perturbations, setting $F_0 = 0.1$ throughout the simulations. In Fig. 11 we plot the numerical results at a fixed time τ, when $\alpha_1 = 0.1$ and α_2 is varied. We see that an increase of α_2 for a fixed value of α_1 causes an increase in amplitudes of pulses in the soliton-crystal structure. To check the oscillating features of the amplitude, width, and repetition rate (hence the position) of the soliton crystal, predicted by the collective-coordinate approach, we also generated numerical solutions of Eq. (46) at four different times. The four graphs shown in Fig. 12 clearly indicate that the soliton-crystal amplitude, width as well as repetition rate are changing with time. Particularly the extreme right and extreme left graphs are regular and similar, reminiscent of periodic oscillations of these characteristic parameters with time.

VI. CONCLUSION

Optical frequency combs stem from outstanding progress achieved over the last two decades in precision control and stabilization of mode-locked ultrafast lasers. Soliton combs [15–17] in particular have emerged as cavity solitons [45] consisting of a regular comb of sharp pulse lines, produced by mode-locked lasers from femtosecond optical frequency comb generators. These specific laser patterns have revolutionized optical frequency metrology and synthesis, they serve as basis for demonstrations of atomic clocks that utilize an optical

frequency transition and have recently shown efficiencies in time-domain applications, including phase-sensitive extreme nonlinear optics and pulse manipulation as well as control [10,46–49].

The aim of the present work is to propose an extensive study of the mechanism of generation and the dynamics of soliton combs in ring-shaped optical microresonators, within the framework of the Lugiato-Levefer equation. Being a specific form of perturbed cubic nonlinear Schrödinger equation, it is ready to assume that the solitonic feature of pulses composing the soliton comb arises from the NLSE while the perturbation, related to the cavity loss and the pump fields, are expected to determine the comb dynamics. Based on this consideration we first address the issue of the generation of soliton-crystal structures that have recently been observed in monolithic Kerr optical frequency comb microresonators. We establish that these structures, which have previously been represented as a periodic train of spatially entangled pulses, are equivalent to the elliptic-soliton solution to the homogeneous NLSE governing equally their pulse components. We analyze the stability of the elliptic soliton and obtained a rich bound-state spectrum consisting of unstable as well as stable long-term internal oscillations existing in the elliptic-soliton backgound. A collective-coordinate approach to the Lugiato-Lefever equation was developed, and numerical simulations were carried out to point out the effects of loss and pump detuning on the elliptic-soliton profiles. In particular, we find that while the time evolution of the elliptic-soliton amplitude is dominantly oscillatory, a variation of the two perturbation parameters gives rise to a quite rich dynamics including rolling patterns and chaotic evolutions.

The values of α_1 and α_2 that were considered in the numerical analysis of Sec. V, actually underscore only a very little aspect of the extremely rich dynamics of the system. Nevertheless, the few values considered provide a valuable insight onto the system dynamics, as reflected in time series of the elliptic-soliton amplitude and the associate phase portraits, as well as the time variation of the elliptic-soliton energy.

[1] Y. S. Kivshar and G. P. Agrawal, *Optical Solitons: From Fibers to Photonic Crystals* (Academic Press, Amsterdam, 2003).

[2] M. H. Weik, *Fiber Optics Standard Dictionary*, 1st ed. (Springer, Reston, VA, 1989).

[3] J. D. Joannopoulos, S. G. Johnson, J. N. Winn, and R. D. Meade, *Photonic Crystals: Molding the Flow of Light*, 2nd ed. (Princeton University Press, Princeton, NJ, 2008).

[4] R. Holzwarth, Th. Udem, T. W. Hansch, J. C. Knight, W. J. Wadsworth, and P. St. J. Russell, Phys. Rev. Lett. **85**, 2264 (2000).

[5] T. W. Hänsch, Rev. Mod. Phys. **78**, 1297 (2006).

[6] P. Del'Haye, A. Schliesser, O. Arcizet, T. Wilken, R. Holzwarth, and T. J. Kippenberg, Nature **450**, 1214 (2007).

[7] E. M. Dianov, P. V. Mamyshev, A. M. Prokhorov, and S. V. Chernikov, Opt. Lett. **14**, 1008 (1989).

[8] J. M. Dudley, F. Gutty, S. Pitois, and G. Millot, IEEE J. Quantum Elect. **37**, 587 (2001).

[9] S. Pitois, J. Fatome, and G. Millot, Opt. Lett. **27**, 1729 (2002).

[10] J. Ye and S. T. Cundiff, *Femtosecond Optical Frequency Comb: Principle, Operation and Applications*, 1st ed. (Springer, Boston, 2005).

[11] M. T. Murphy, T. Udem, R. Holzwarth, A. Sizmann, L. Pasquini, and C. Araujo-Hauck, Mon. Not. R. Astron. Soc. **380**, 839 (2007).

[12] B. A. Malomed, A. Schwache, and F. Mitschke, Fib. Integr. Opt. **17**, 267 (1998).

[13] M. Zajnulina, M. Böhm, D. Bodenmüller, J. M. Chavez Boggio, A. A. Rieznik, and M. M. Roth, Opt. Commun. **393**, 95 (2017).

[14] C. Godey, I. V. Balakireva, A. Coillet, and Y. K. Chembo, Phys. Rev. A **89**, 063814 (2014).

[15] Y. V. Kartashov, O. Alexander, and D. V. Skryabin, Opt. Express **25**, 11550 (2017).

[16] N. G. Pavlov, G. Lihachev, S. Koptyaev, E. Lucas, M. Karpov, N. M. Kondratiev, I. A. Bilenko, T. J. Kippenberg, and M. L. Gorodetsky, Opt. Lett. **42**, 514 (2017).

[17] M. H. P. Pfeiffer, C. Herkommer, J. Liu, H. Guo, M. Karpov, E. Lucas, M. Zervas, and T. J. Kippenberg, Optica **4**, 684 (2017).

[18] Y. K. Chembo and C. R. Menyuk, Phys. Rev. A **87**, 053852 (2013).

[19] F. Amrani, A. Niang, M. Salhi, A. Komarov, H. Leblond, and F. Sanchez, Opt. Lett. **36**, 4239 (2011).

[20] A. Haboucha, H. Leblond, M. Salhi, A. Komarov, and F. Sanchez, Phys. Rev. A **78**, 043806 (2008).

[21] A. Haboucha, H. Leblond, M. Salhi, A. Komarov, and F. Sanchez, Opt. Lett. **33**, 524 (2008).

[22] F. Amrani, M. Salhi, P. Grelu, H. Leblond, and F. Sanchez, Opt. Lett. **36**, 1545 (2011).

[23] D. C. Cole, E. S. Lamb, P. Del'Haye, S. A. Diddams, and P. B. Scott, Nat. Photon. **11**, 671 (2017).

[24] A. M. Dikandé, Phys. Rev. A **81**, 013821 (2010).

[25] L. A. Lugiato and R. Lefever, Phys. Rev. Lett. **58**, 2209 (1987).

[26] T. Herr, V. Brasch, J. D. Jost, C. Y. Wang, N. M. Kondratiev, M. L. Gorodetsky, and T. J. Kippenberg, Nat. Photon. **8**, 145 (2014).

[27] D. J. Fandio Jubgang and A. M. Dikandé, J. Opt. Soc. Am. B **34**, 66 (2017).

[28] Z. Qi, D. Giuseppe, and C. R. Menyuk, J. Opt. Soc. Am. B **34**, 785 (2017).

[29] D. J. Fandio Jubgang, A. M. Dikande, and A. Sunda-Meya, Phys. Rev. A **92**, 053850 (2015).

[30] R. A. Sack, J. Inst. Maths. Applic. **10**, 279 (1972).

[31] H. Luther, Math. Comp. **22**, 434 (1968).

[32] D. Sarafyan, J. Math. Anal. Applic. **40**, 436 (1972).

[33] N. N. Akhmediev, V. M. Eleonskii, and N. E. Kulagin, Theor. Math. Phys. **72**, 809 (1987).

[34] A. M. Dikandé, J. Opt. **13**, 035203 (2011).

[35] D. S. Mbieda Petmegni, A. M. Dikandé, and B. Z. Essimbi, Appl. Phys. B **123**, 171 (2017).

[36] D. S. Mbieda Petmegni and A. M. Dikandé, J. Mod. Opt. **64**, 1192 (2017).

[37] D. E. Pelinovsky, Y. S. Kivshar, and V. V. Afanasjev, Physica D **116**, 121 (1998).

[38] F. M. Arscott and I. M. Khabaza, *Tables of Lamé Polynomials, Mathematical Tables Series* (Pergamon Press, Oxford, 1962).

[39] A. M. Dikandé, Phys. Scr. **60**, 291 (1999).

[40] J. M. Soto-Crespo, N. Devine, and N. Akhmediev, Phys. Rev. A **96**, 023825 (2017).

[41] Y. S. Kivshar and B. A. Malomed, Rev. Mod. Phys. **61**, 763 (1989).

[42] W. H. Press, S. A. Teukolsky, W. T. Vetterling, and B. P. Flannery, *Numerical Recipes in C*, 3rd ed. (Cambridge University Press, New York, 2007).

[43] Y. Chembo, Nanophotonics **5**, 214 (2016).

[44] J. A. C. Weideman and B. M. Herbst, SIAM J. Numer. Anal. **23**, 485 (1986).

[45] L. Spinelli, G. Tissoni, M. Tarenghi, and M. Brambilla, Eur. Phys. J. D **15**, 257 (2001).

[46] P. Monot, T. Auguste, P. Gibbon, F. Jakober, G. Mainfray, A. Dulieu, M. Louis-Jacquet, G. Malka, and J. L. Miquel, Phys. Rev. Lett. **74**, 2953 (1995).

[47] J. S. De Groot, K. G. Estabrook, W. L. Kruer, R. P. Drake, K. Mizuno, and S. M. Cameron, Phys. Fluids B **4**, 701 (1992).

[48] R. R. Freeman, P. H. Bucksbaum, H. Milchberg, S. Darack, D. Schumacher, and M. E. Geusic, Phys. Rev. Lett. **59**, 1092 (1987).

[49] H. Zhang, S. M. Eaton, and P. R. Herman, Opt. Lett. **32**, 2559 (2007).